Birkbeck
UNIVERSITY OF LONDON

BIROn - Birkbeck Institutional Research Online

Hin, R. and Coath, C. and Carter, P. and Nimmo, F. and Lai, Y.-J. and Pogge von Strandmann, Philip A.E. and Willbold, M. and Leinhardt, Z. and Walter, M. and Elliott, T. (2017) Magnesium isotope evidence that accretional vapour loss shapes planetary compositions. Nature 549 , pp. 511-514. ISSN 0028-0836.

Downloaded from: https://eprints.bbk.ac.uk/id/eprint/20168/

Usage Guidelines:
Please refer to usage guidelines at https://eprints.bbk.ac.uk/policies.html or alternatively contact lib-eprints@bbk.ac.uk.

Magnesium isotope evidence that accretional vapour loss shapes planetary compositions

Remco C. Hin[1], Christopher D. Coath[1], Philip J. Carter[2,4], Francis Nimmo[3], Yi-Jen Lai[1,5], Philip A.E. Pogge von Strandmann[1,6], Matthias Willbold[1,7], Zoë M. Leinhardt[2], Michael J. Walter[1], Tim Elliott[1]

[1]*School of Earth Sciences, University of Bristol, Wills Memorial Building, Queen's Road, Bristol BS8 1RJ, UK; remco.hin@bristol.ac.uk*

[2]*School of Physics, University of Bristol, H. H. Wills Physics Laboratory, Tyndall Avenue, Bristol BS8 1TL, UK*

[3]*Department of Earth and Planetary Sciences, University of California Santa Cruz, Santa Cruz CA 95064, USA*

[4]*Now at: Department of Earth and Planetary Sciences, University of California Davis, One Shields Avenue, Davis CA 95616, USA*

[5]*Now at: Macquarie University GeoAnalytical, Department of Earth and Planetary Sciences, Macquarie University, 12 Wally's Walk, Sydney NSW 2109, Australia*

[6]*Now at: London Geochemistry and Isotope Centre, Department of Earth Sciences, University College London, and Department of Earth and Planetary Sciences, Birkbeck, University of London, Gower Street, London WC1E 6BT, UK*

[7]*Now at: Geowissenschaftliches Zentrum Göttingen (GZG), University of Göttingen, Goldschmidtstr. 1, 37077 Göttingen, Germany*

Introductory paragraph

It has long been recognised that Earth and other differentiated planetary bodies are chemically fractionated compared to primitive, chondritic meteorites and by inference the primordial disk from which they formed. An important question has been whether the notable volatile depletions of planetary bodies are a consequence of accretion[1], or inherited from prior nebular fractionation[2]. The isotopic compositions of the main constituents of planetary bodies can contribute to this debate[3-6]. Using a new analytical approach to address key issues of accuracy inherent in conventional methods, we show that all differentiated bodies have isotopically heavier magnesium compositions than chondritic meteorites. We argue that possible magnesium isotope fractionation during condensation of the solar nebula, core formation and silicate differentiation cannot explain these observations. However, isotopic fractionation between liquid and vapour followed by vapour escape during accretionary growth of planetesimals generates appropriate residual compositions. Our modelling implies that the isotopic compositions of Mg, Si and Fe and the relative abundances of the major

elements of Earth, and other planetary bodies, are a natural consequence of substantial (~40% by mass) vapour loss from growing planetesimals by this mechanism.

Main text

Magnesium is a fundamental building block of the terrestrial planets, constituting ~15% of Earth's mass. Compared to the 'solar' composition of the primordial disk, it is well established that the Earth is depleted in Mg by ~20% relative to more cosmochemically refractory elements (e.g. Al), consistent with increasing terrestrial depletions of elements with higher volatility (e.g. ref [7]). Mass-dependent isotopic fractionations of other major elements, Si and Fe, have been used to argue for compositional modification by accretional vapour loss[3,6]. Yet contrasting conclusions have been derived from similar observations in studies that point to fractionations occurring for these elements during planetary differentiation[8,9]. In this respect, the isotopic composition of Mg may be better suited to interrogate chemical fractionation in the Solar System[5]. However, detecting mass-dependent isotopic differences between primitive chondrites and differentiated bodies poses significant analytical challenges because only small (<<1‰/amu) fractionations typically occur during the high temperature processes (>1300 K) that shape planetary evolution. Indeed, various comparisons of terrestrial and chondritic Mg isotope ratios have reached opposing conclusions as to whether or not the Earth is chondritic[5,10-17]. Much of the divergent opinion appears to stem from difficulties in achieving sufficiently accurate measurements[18].

In Figure 1a we illustrate that a number of different studies report chondritic $^{25}Mg/^{24}Mg$ ~0.03-0.05‰ lower than the Earth[5,10-12], but in only one case do the authors actually argue that the Earth is non-chondritic[5]. Reliable resolution of such small isotopic differences requires tight control on analytical artefacts. Of particular concern is that samples and standards behave slightly differently during analysis, despite prior purification. Unlike the traditional sample-standard bracketing approach, the method of double-spiking explicitly corrects such behaviour, but it is not standard for elements with only three stable isotopes, like magnesium. We have, therefore, developed a new approach of "critical mixture double spiking" to overcome this problem[19] (see Methods for details). Based on propagation of conservative estimates of systematic error, this method has a limiting accuracy

59 <0.005‰/amu[19]. Repeat measurements of solution standards and geological reference materials
60 indicate that we can achieve reproducibilities of ±0.010‰ (2se) for octuple measurements.
61 We have measured the Mg isotope compositions of a range of terrestrial rocks and primitive and
62 differentiated meteorites using critical mixture double spiking (Table 1). As shown in Figure 1b,c, our
63 new data substantiate that chondrites have $^{25}Mg/^{24}Mg$ ~0.02‰ lower than the differentiated Earth,
64 Mars, eucrite and angrite parent bodies.
65 Visual (Figure 1b) and statistical (see Methods) inspection shows some data scatter. For terrestrial
66 samples this is mostly due to two ocean island basalts (OIB), whose sources likely contain recycled
67 components, originally fractionated at Earth's surface. However, we focus on analyses of mantle
68 peridotites to estimate the composition of bulk Earth more robustly. Mg isotope variability among
69 chondrites is foremost within the carbonaceous group. This scatter is readily explained by variable
70 parent body aqueous alteration, as their $^{25}Mg/^{24}Mg$ vary systematically with oxygen isotope
71 compositions[20] and petrographic class (Extended Data Figure 1) in the sense anticipated from
72 terrestrial weathering[21]. Removing these anomalous samples, we document a statistically significant
73 difference in Mg isotope compositions between chondrites and the variably-sized, differentiated
74 bodies of Earth, Mars and the eucrite parent body (p_{ANOVA} 1.5×10^{-6}). If enstatite chondrites are
75 considered separately from other chondrites ($p_{t\text{-}test}$ 0.017), their mean $^{25}Mg/^{24}Mg$ is also significantly
76 lighter than differentiated bodies (~0.013‰; p_{ANOVA} 7.8×10^{-4}). In contrast, the differentiated bodies are
77 statistically indistinguishable from each other (p_{ANOVA} 0.16).
78 The lack of systematic differences in $^{25}Mg/^{24}Mg$ between melt-depleted harzburgites, fertile
79 lherzolites and mid-ocean ridge basalts reaffirm, at higher precision, previous observations[12] that Mg
80 isotopes do not fractionate discernibly during (ultra)mafic silicate differentiation (Figure 1, Table 1
81 and Extended Data Figure 2). Silicate differentiation is, therefore, not responsible for the relatively
82 heavy Mg isotope compositions of our samples of differentiated planetary bodies.
83 Although the difference in $^{25}Mg/^{24}Mg$ between Earth and primitive meteorites is small, bulk
84 perturbation of such an abundant element requires the operation of planetary scale processes. Core
85 formation cannot account for this observation, because unlike Fe and Si, Mg only becomes siderophile
86 at temperatures too high for significant isotopic fractionation[22]. Vapour fractionation typically

produces larger isotopic differences than magmatic processes. Such fractionation may have occurred during initial condensation of solids from the cooling proto-solar nebula, as has been invoked to explain variability between meteoritic and planetary silicon isotope compositions[4]. Yet, such a model predicts the low Mg/Si enstatite chondrites should have the lowest $^{25}Mg/^{24}Mg$ of the primitive meteorites. This is inconsistent with our observations, in which enstatite chondrites have the isotopically heaviest Mg of the anhydrous chondrites and the Earth, moreover, is distinct from chondrites.

Instead, we propose that differentiated planetary bodies obtained their relatively heavy Mg isotope compositions by vapour-melt fractionation following impacts during accretionary growth of planetesimals. Loss of vapour, which was subsequently swept into the Sun or blown beyond the zone of accretion, would leave residual planetary bodies isotopically heavy. Vapour loss is most effective for bodies <~0.1 Earth masses ($M_\oplus$) as escape velocities of larger bodies are mostly too high to be exceeded by silicate vapour molecules (see Supplementary Information). We posit that vapour loss signatures were abundantly imparted to small bodies in the inner Solar System, as evidenced by our analyses of silicate achondrites (Figure 1b). Larger bodies like Earth dominantly accreted from such vapour depleted planetesimals, thereby inheriting their signatures.

Although small bodies can readily lose vapour, low mutual impact velocities limit the amount of vapour produced directly during these early stages of accretion. To investigate this quantitatively, we have post-processed the results of previously published, high-resolution N-body simulations[23] (see Methods for details) using a parameterisation of impact-induced vaporisation[4]. In this model, cumulative vapour produced increases from <1 to ~20% of a body's final mass for bodies from 10^{-4} to 10^{-1} $M_\oplus$ (Figure 2a). As an alternative approach we have calculated vapour mass loss by direct outflow of silicate vapour from the surface of impact-generated magma ponds/oceans (see Supplementary Information for details). Although magma oceans may have been produced by radiogenic heating (e.g. ^{26}Al decay), we conservatively focussed on converting impact velocities of the same N-body simulations to energy available for melting/vapour outflow. We obtain cumulative

vapour mass losses of ~4-36% for bodies with 10^{-4} to 10^{-1} $M_{\oplus}$ final masses (Figure 2b). Given the higher mass losses from smaller bodies in the second, magmatic scenario we focus on this process.

The outflow velocities of vapour above the magma ponds/oceans are sufficiently high that this mechanism is not mass discriminative. This implies that isotopic fractionation only occurs during production of vapour at the surface of the magma pond/ocean. We treat this as an equilibrium process between a molten surface and transient atmosphere, as vapour-liquid chemical equilibrium is attained rapidly[24]. Furthermore, kinetic isotope fractionation in this scenario can be ruled out empirically from consideration of marked effects on K isotope ratios that are unobserved in nature[25] (see Methods).

We have modelled Mg, Si and Fe equilibrium isotope fractionation between a liquid and vapour with compositions calculated using thermodynamic data for a nine-component system of major and minor elements of variable volatility (see Methods for details). To obtain a residual planetesimal with a Mg isotope composition ~0.02‰ higher than our average chondritic value, our model predicts ~0.30‰ and ~0.013‰ super-chondritic $^{30}Si/^{28}Si$ and $^{56}Fe/^{54}Fe$ (Figure 3a). These values are largely compatible with the Earth (Figure 3) and several other bodies (Extended Data Figure 3), despite some currently rather poorly constrained input parameters (see Methods); refinement of these values may resolve these minor mismatches. Starting more specifically with an enstatite chondrite composition, as thought most isotopically appropriate for Earth (e.g. ref [26]), ~47% of the body is vaporised and lost, which removes ~14% of the initial Mg mass together with ~65% Si, ~48% Fe and >99.9% of Na and K (Figure 3c). Similar total mass losses were deduced previously for Earth[27] from the volatilities of major constituents based on a comparison to vaporisation experiments. The total mass losses inferred from these chemical constraints (Figure 3) are reassuringly similar to those calculated from our physical model of vapour loss (Figure 2b).

The predicted elemental losses modify the composition of enstatite chondrites into one similar to the Earth's (Figure 3c,d), without requiring substantial, preferential collisional erosion of a putative crust formed by small degrees melts of an undifferentiated body[28]. Our modelled vapour-loss modification resolves the conundrum that Earth's isotopic anomalies suggest a close genetic link to enstatite chondrites despite vastly different elemental compositions[26]. Close matches to Earth's composition are also obtained, however, when starting with e.g. a CI chondrite composition (Extended

Data Figure 4). While potassium depletion relative to chondrites in eucrite (>94%) and angrite (>99%) parent bodies[25] is comparable to our vapour depletion model results, it requires re-accretion of ~20% chondritic material to match terrestrial alkali abundances. This material can be derived from the distribution tail of bodies that escape melting and vapour loss.

Our vapour loss model quantitatively accounts for non-chondritic abundances and isotopic compositions of major elements as a natural consequence of planetary accretion and provides a viable mechanism for previous suggestions of the importance of evaporative losses in planetary evolution[3,6,27,29]. This process inevitably results in dramatic loss of elements more volatile than Mg. Planetary compositions thus intrinsically reflect their history of collisional formation.

Main references

1 Ringwood, A. E. Chemical Evolution of the Terrestrial Planets. *Geochim. Cosmochim. Acta* **30**, 41-104, doi:10.1016/0016-7037(66)90090-1 (1966).

2 Anders, E. Chemical Processes in the Early Solar System, as Inferred from Meteorites. *Accounts Chem Res* **1**, 289-298, doi:10.1021/ar50010a001 (1968).

3 Pringle, E. A., Moynier, F., Savage, P. S., Badro, J. & Barrat, J. A. Silicon isotopes in angrites and volatile loss in planetesimals. *Proc. Natl. Acad. Sci., USA* **111**, 17029-17032, doi:10.1073/pnas.1418889111 (2014).

4 Dauphas, N., Poitrasson, F., Burkhardt, C., Kobayashi, H. & Kurosawa, K. Planetary and meteoritic Mg/Si and δ^{30}Si variations inherited from solar nebula chemistry. *Earth Planet. Sci. Lett.* **427**, 236-248, doi:10.1016/j.epsl.2015.07.008 (2015).

5 Young, E. D., Tonui, E., Manning, C. E., Schauble, E. & Macris, C. A. Spinel-olivine magnesium isotope thermometry in the mantle and implications for the Mg isotopic composition of Earth. *Earth Planet. Sci. Lett.* **288**, 524-533, doi:10.1016/j.epsl.2009.10.014 (2009).

6 Poitrasson, F., Halliday, A. N., Lee, D. C., Levasseur, S. & Teutsch, N. Iron isotope differences between Earth, Moon, Mars and Vesta as possible records of contrasted accretion mechanisms. *Earth Planet. Sci. Lett.* **223**, 253-266, doi:10.1016/j.epsl.2004.04.032 (2004).

7 Palme, H. & O'Neill, H. S. C. in *The Mantle and Core* Vol. 2 *Treatise on Geochemistry* (ed R. W. Carlson) (Elsevier-Pergamon, 2003).

8 Weyer, S. & Ionov, D. A. Partial melting and melt percolation in the mantle: The message from Fe isotopes. *Earth Planet. Sci. Lett.* **259**, 119-133, doi:10.1016/j.epsl.2007.04.033 (2007).

9 Georg, R. B., Halliday, A. N., Schauble, E. A. & Reynolds, B. C. Silicon in the Earth's core. *Nature* **447**, 1102-1106, doi:10.1038/Nature05927 (2007).

10 Bourdon, B., Tipper, E. T., Fitoussi, C. & Stracke, A. Chondritic Mg isotope composition of the Earth. *Geochim. Cosmochim. Acta* **74**, 5069-5083, doi:10.1016/j.gca.2010.06.008 (2010).

11 Pogge von Strandmann, P. A. E. *et al.* Variations of Li and Mg isotope ratios in bulk chondrites and mantle xenoliths. *Geochim. Cosmochim. Acta* **75**, 5247-5268, doi:10.1016/j.gca.2011.06.026 (2011).

12 Teng, F. Z. *et al.* Magnesium isotopic composition of the Earth and chondrites. *Geochim. Cosmochim. Acta* **74**, 4150-4166, doi:10.1016/j.gca.2010.04.019 (2010).

13 Wiechert, U. & Halliday, A. N. Non-chondritic magnesium and the origins of the inner terrestrial planets. *Earth Planet. Sci. Lett.* **256**, 360-371, doi:10.1016/j.epsl.2007.01.007 (2007).

14 Bizzarro, M. *et al.* High-precision Mg-isotope measurements of terrestrial and extraterrestrial material by HR-MC-ICPMS–implications for the relative and absolute Mg-isotope composition of the bulk silicate Earth. *J. Anal. At. Spectrom.* **26**, 565-577, doi:10.1039/C0ja00190b (2011).
15 Handler, M. R., Baker, J. A., Schiller, M., Bennett, V. C. & Yaxley, G. M. Magnesium stable isotope composition of Earth's upper mantle. *Earth Planet. Sci. Lett.* **282**, 306-313, doi:10.1016/j.epsl.2009.03.031 (2009).
16 Chakrabarti, R. & Jacobsen, S. B. The isotopic composition of magnesium in the inner Solar System. *Earth Planet. Sci. Lett.* **293**, 349-358, doi:10.1016/j.epsl.2010.03.001 (2010).
17 Yang, W., Teng, F. Z. & Zhang, H. F. Chondritic magnesium isotopic composition of the terrestrial mantle: A case study of peridotite xenoliths from the North China craton. *Earth Planet. Sci. Lett.* **288**, 475-482, doi:10.1016/j.epsl.2009.10.009 (2009).
18 Teng, F. Z. *et al.* Interlaboratory comparison of magnesium isotopic compositions of 12 felsic to ultramafic igneous rock standards analyzed by MC-ICPMS. *Geochem. Geophy. Geosy.* **16**, 3197-3209, doi:10.1002/2015gc005939 (2015).
19 Coath, C. D., Elliott, T. & Hin, R. C. Double-spike inversion for three-isotope systems. *Chem. Geol.* **451**, 78-89, doi:10.1016/j.chemgeo.2016.12.025 (2017).
20 Clayton, R. N. & Mayeda, T. K. The oxygen isotope record in Murchison and other carbonaceous chondrites. *Earth Planet. Sci. Lett.* **67**, 151-161, doi:10.1016/0012-821x(84)90110-9 (1984).
21 Tipper, E. T. *et al.* The magnesium isotope budget of the modern ocean: Constraints from riverine magnesium isotope ratios. *Earth Planet. Sci. Lett.* **250**, 241-253, doi:10.1016/j.epsl.2006.07.037 (2006).
22 O'Rourke, J. G. & Stevenson, D. J. Powering Earth's dynamo with magnesium precipitation from the core. *Nature* **529**, 387-389, doi:10.1038/nature16495 (2016).
23 Carter, P. J., Leinhardt, Z. M., Elliott, T., Walter, M. J. & Stewart, S. T. Compositional Evolution during Rocky Protoplanet Accretion. *Astrophys. J.* **813**, doi:10.1088/0004-637x/813/1/72 (2015).
24 Fegley, B. & Schaefer, L. in *The atmosphere - History* Vol. 6 *Treatise on Geochemistry* (ed J. Farquhar) Ch. 6.3, 406 (Elsevier, 2013).
25 Humayun, M. & Clayton, R. N. Potassium isotope cosmochemistry: Genetic implications of volatile element depletion. *Geochim. Cosmochim. Acta* **59**, 2131-2148, doi:10.1016/0016-7037(95)00132-8 (1995).
26 Javoy, M. *et al.* The chemical composition of the Earth: Enstatite chondrite models. *Earth Planet. Sci. Lett.* **293**, 259-268, doi:10.1016/j.epsl.2010.02.033 (2010).
27 Young, E. D. Assessing the implications of K isotope cosmochemistry for evaporation in the preplanetary solar nebula. *Earth Planet. Sci. Lett.* **183**, 321-333, doi:10.1016/S0012-821x(00)00276-4 (2000).
28 Boujibar, A., Andrault, D., Bolfan-Casanova, N., Bouhifd, M. A. & Monteux, J. Cosmochemical fractionation by collisional erosion during the Earth's accretion. *Nature Communications* **6**, doi:10.1038/ncomms9295 (2015).
29 Pringle, E. A. & Moynier, F. Rubidium isotopic composition of the Earth, meteorites, and the Moon: Evidence for the origin of volatile loss during planetary accretion. *Earth Planet. Sci. Lett.* **473**, 62-70, doi:10.1016/j.epsl.2017.05.033 (2017).
30 Walsh, K. J., Morbidelli, A., Raymond, S. N., O'Brien, D. P. & Mandell, A. M. Populating the asteroid belt from two parent source regions due to the migration of giant planets–"The Grand Tack". *Meteorit. Planet. Sci* **47**, 1941-1947, doi:10.1111/j.1945-5100.2012.01418.x (2012).
31 Wasson, J. T. & Kallemeyn, G. W. Compositions of Chondrites. *Philos T Roy Soc A* **325**, 535-544 (1988).

Acknowledgements

We thank the Natural History Museum in London, NASA, Oliver Nebel, Dmitri Ionov, Sune Nielsen, Eiichi Takazawa, Ken Sims, Yaoling Niu, Richard Brooker, Cynthia Robinson for supplying us with a variety of samples. We acknowledge Carver Bierson for his help with direct outflow vapour loss modelling. This study was funded by NERC grant NE/L007428/1 to TE, CDC and MJW, which was motivated by NE/C0983/1. ERC Adv Grant 321209 ISONEB further supported the work of TE and CDC. NERC grant NE/K004778/1 to ZL funded PC.

Author contributions

All data presented were measured by RH. RH and CDC performed vapour-liquid modelling. PC was responsible for calculations relating to N-body simulations, FN modelled the direct outflow vapour loss mechanism. RH and TE wrote the manuscript. CDC, YJL, PPvS and MW were involved in measurements in the initial stages of this study. All authors read and commented on the manuscript.

Author Information

Reprints and permissions information is available at www.nature.com/reprints. The authors declare no competing financial interests. Correspondence and requests for materials should be addressed to remco.hin@bristol.ac.uk.

255

256 ***Figure captions***

257 Figure 1. Magnesium isotope compositions. a) Probability density plots of Mg isotope
258 compositions from previous standard-sample bracketing work, highlighting the results of individual
259 studies[5,10-12] that presented numerous analyses of both terrestrial and chondritic samples using the
260 same methodology. These data show systematic subtle differences (0.02-0.05‰) between the Earth
261 and primitive meteorites. Typically authors refrained from interpreting such small differences. b)
262 Samples from this study (measured by critical mixture double spiking) ordered according to sample-
263 type. Lines and shaded bars indicate means and 2se. Samples displayed with pale symbols are
264 excluded from means (see main text). c) Earth and chondrite analyses from b) shown as probability
265 plot to compare with a).

266

267 Figure 2. Median cumulative vapour fractions produced as a function of final planetary mass (in
268 Earth masses $M_{\oplus}$) determined from high-resolution N-body simulations of planetary accretion[23]. The
269 N-body simulations encompassed two scenarios: a calm disk without gas drag ("calm") and a disk that
270 is disturbed by a Grand Tack motion of Jupiter[30] ("GT"). a) Vapour loss fractions calculated for
271 impact vaporisation parameterised to impact velocity[4]. b) Vapour loss fractions produced by direct
272 outflow above exposed magma ponds/oceans. In a Grand Tack scenario, Jupiter's motions cause
273 higher eccentricities and hence higher impact velocities for such small bodies, which explains their
274 high vapour fractions.

275

276 Figure 3. Comparison between modelled compositions of a vapour depleted liquid and observed
277 terrestrial compositions. a) Changes in isotope compositions (‰/amu) against total relative vapour
278 loss (F_{Total}, in mole fractions) calculated in our model. b) Observed terrestrial Mg (this study), and Si
279 (from [4] and references therein) isotope compositions relative to enstatite chondrites (EH). Errors are
280 2se. c) Loss (mole fraction) of a given element (X), f_X, versus F_{Total}. d) Molar element/Ca of the
281 terrestrial mantle[7], normalised to EH[31]. Shaded bands give error bounds for F_{Total} inferred from Mg
282 isotope data and the intersection of different curves with this field indicates the range of terrestrial
283 depletions predicted for our vapour loss model. Comparison of these values to those calculated for the
284 Earth relative to an enstatite chondrite starting composition (b and d) is generally good, despite
285 uncertainties in model input parameters (see Methods) and additional influences on observed values
286 from nebular and core formation processes[4,9]. Left pointing arrows show the effect of post-volatile loss
287 accretion of 20% chondrite (EH).

288

289

290 **Methods**

291 *Chemical and analytical protocols, and data statistics*

292 Powdered samples were digested in cleaned Savillex PFA beakers with 3:1 ultra-pure ~15.5M
293 HNO_3 and ~28M HF. Prior to drying, ~0.5 ml 7M $HClO_4$ was added to prevent precipitation of
294 insoluble fluorides. At this stage, insoluble chromites were visible in some peridotites. They were
295 separated from the supernatant and further digested in high-pressure acid digestion vessels (Anton
296 Paar Asher) before being re-combined with the rest of the digested sample. Similarly, graphite
297 precipitates were removed from enstatite chondrites by transferring the samples into pre-cleaned BN
298 crucibles that were placed in a muffle furnace at 600 °C, making use of the phase transition of graphite
299 to CO_2 under these conditions. Following complete digestion, any remaining organic components were
300 attacked with ~15.5M HNO_3 and 30% H_2O_2. Terrestrial samples generally weighed 2-15 mg, while
301 larger meteorite samples were dissolved (~7-150 mg, majority 60-100 mg; see Extended Data Table 1)
302 to obtain representative samples.

303 Magnesium was separated from the sample matrix with a Biorad AG50W-X12 cationic exchange
304 resin and 2M HNO_3 eluent as described previously[11]. Yields were monitored and were >99.85% for all
305 analysed samples. Following separation, samples were dissolved in 0.3M HNO_3 and critically double
306 spiked (see below) for analyses on a Thermo Finnigan Neptune (s/n 1020) multi-collector inductively
307 coupled plasma mass spectrometer (MC-ICPMS). A Savillex PFA nebuliser (30-40 μl min^{-1} uptake)
308 aspirated the sample solution into an Elemental Scientific Inc. Apex HF introduction system prior to
309 ionisation in the plasma. A combination of Jet sampler and H skimmer cones was used and Mg masses
310 24, 25 and 26 were collected in cups L4, centre and H4, respectively. The Neptune was further
311 operated in medium resolution mode ($M/\Delta M \geq 4000$, 5-95% peak height definition) with an off-peak
312 centre mass (^{25}Mg mass 24.979 instead of 24.986) to resolve any minor possible $^{12}C^{14}N^+$ interferences
313 on $^{26}Mg^+$. However, these interferences should be insignificant as they were observed to be only ~15
314 ppm of the $^{26}Mg^+$ signal. This medium resolution mode also improved signal-to-noise ratios, reducing
315 total background signals to $<2\times10^{-13}$ A. A 10^{11} Ω feedback resistor was used in the amplifier
316 connected to the centre cup, while 10^{10} Ω resistors were used on L4 and H4. Total Mg intensities of
317 ~2×10^{-9} A were measured at total Mg concentrations of ~2.5 μg ml^{-1} for 168 s integration (20 cycles of
318 8.4 s), consuming ~185 ng sample Mg per analysis in double-spiked samples.

319 A measurement sequence typically consisted of analysis of a mixture of double spike and DSM-3
320 reference standard followed by three sample – double-spike mixtures, repeating until all samples were
321 measured before starting this series again to make duplicate analyses of samples. Normally, double-
322 spike – sample mixture measurements were repeated four times per sequence, in which a total of 9-17
323 samples were measured. Sequences were repeated in different analysis sessions over the course of the
324 study to yield at least 8 repeated analyses of each double-spike – sample mixture. All sample and
325 standard analyses were preceded by a 240 s wash-out and an on-peak background measurement (168 s
326 integration). The mean intensities of the latter were subtracted from the intensities of the sample or

standard analysis that followed it. Additionally, three analyses of unspiked DSM-3 (the concentration matched to the double-spike – sample mixtures) were performed before, after and in the middle of the sequence of double-spike – sample (or standard) mixtures. A 15 minute wash-out was performed between these unspiked and spiked analyses because the Mg isotope composition of the background greatly changes as a consequence of switching between spiked and unspiked analyses, which makes critical mixture double spiking more prone to added variability due to background corrections. In our analyses, background corrections usually affected the reported isotope compositions by <0.0005‰, which is well below the uncertainties of 0.008-0.010‰. Sequences typically took ~10-20 hours.

Interferences by hydrides (i.e. $^{24}MgH^+$ on $^{25}Mg^+$ and $^{25}MgH^+$ on $^{26}Mg^+$), which are difficult to fully resolve, as well background Mg intensities were reduced by using a -1 kV extraction voltage instead of the default -2 kV. We observed that such a change in the extraction voltage reduces background $^{24}MgH^+$ and $^{25}MgH^+$ intensities by ~10 times, i.e. ~500 cps $^{24}MgH^+$ in medium resolution. Simultaneously, the change in extraction voltage lowers background Mg intensities by ~4-5 times, while sample sensitivity is only reduced by <20%. Applying an extraction weaker than -1 kV further decreases backgrounds, but increasingly lowers sensitivity. We interpret these effects as evidence that the background signals are dominantly produced by liberation (with/without hydride) of Mg deposited at the back of the skimmer cone. This hypothesis is substantiated by the fact that progressively increasing Mg background intensities can be lowered by brief cleaning of the back of the skimmer cone with a droplet of dilute HNO_3. Moreover, background Mg isotope compositions are extremely light after mass bias correction with the same instrumental fractionation factor as for sample Mg, suggesting additional mass fractionation. Finally, we observed that hydride intensities increase over background only ~75 fold when Mg intensities are increased ~25'000 fold by introducing sample Mg. We thus estimate that the largest relative hydride intensity contribution to Mg ($^{24}MgH^+/^{25}Mg^+$) is ~13 ppm. Since we externally normalise samples to intensity matched DSM-3 standards (see *Critical mixture double spiking* below), these hydride contributions are reduced to such small levels that they do not affect our reported isotope compositions.

Data in Table 1 are reported as relative differences of isotope ratios to the reference solution standard DSM-3[32] in delta notation following IUPAC recommendations[33]: $\delta^{25/24}Mg = \left(\left({}^{25}Mg/{}^{24}Mg \right)_{Sample} / \left({}^{25}Mg/{}^{24}Mg \right)_{DSM-3} - 1 \right)$. The data are presented in per mil and represent means of repeated analyses. Reported uncertainties are standard error of the mean (*2se*) calculated as $2s/\sqrt{n}$ in which n is the number of repeated analyses for the corresponding sample. Instead of using the standard deviation (s) of a geological reference material (e.g. BHVO-2, $2s$ = 0.029‰, n = 60 from 3 digestions), we determined s by a homoscedastic approach, pooling over all standards and samples[34]. That is, after determining the sums of the squared deviations of n repeated measurements from their m sample (and standard) means, these sums were themselves summed before

dividing by the degrees of freedom (k): $s^2 = \frac{1}{k}\sum_{i=1}^{m}\sum_{j=1}^{n_i}\left(x_{ij} - \overline{x}_i\right)^2$ with $k = \left(\sum_{i=1}^{m} n_i\right) - m$. We obtained $2s$ = 0.029‰ (k = 693) and have found justification in using this scheme because the n repeats of m samples and standards passed the null hypothesis of a Bartlett's test, i.e. the m samples and standards come from normal distributions with the same variance.

Group means (e.g. Earth) and their *2se* uncertainties are calculated directly from the relevant sample data in Table 1. Significances of group mean differences were determined with a one-way Analysis of Variance (one-way ANOVA) or a two sample Student's t-test, again using the relevant data in Table 1. Within group differences were investigated with one-way ANOVA using sample repeat measurements.

Critical mixture double spiking

The analysis routine described above is broadly similar to previous studies performed by standard-sample bracketing. Our contribution to addressing previously observed inter-laboratory inconsistencies[18] resides in the novelty of adding a double-spike prior to mass-spectrometric analysis. As detailed elsewhere[19], this technique of "critical mixture double spiking" corrects for mass bias effects of residual matrix, eliminating the most plausible cause for the inter-laboratory inconsistencies. It helps ensure that analyses are not only precise, but also accurate to within the quoted precision. In practice, we dissolved ^{25}MgO and ^{26}MgO spikes (purchased from Oak Ridge National Laboratory, batch numbers 217201 and 158690, respectively) and mixed them to produce a double spike with ^{24,25,26}Mg abundances of 0.30%, 6.27%, 93.43%, approximating those for an accuracy optimised scenario (0%, 8.4%, 91.6%, respectively[19]). We calibrated this double-spike to reference solution standard DSM-3 following our suggested protocol[19].

After ion exchange chemistry, we aliquoted a weight of separated Mg sufficient for at least 10 runs and mixed this with a weighed amount of double-spike estimated to yield a molar spike proportion of 0.5908 in the mixture. This is the critical mixing proportion for our double-spike composition. Prior to analysis, double-spike – sample mixtures were equilibrated at 100 °C for 2-3 h in closed Savillex PFA autosampler vials. Subsequently, all samples were analysed once by MC-ICPMS in a short sequence to determine their deviation from the critical spike proportion. At this stage, the mixtures were rarely within our acceptable bound of ±0.5% molar proportion from critical. Based on the documented sample and double-spike weights and the observed double-spike proportion, either sample or double-spike was added to the mixtures, followed by another short analysis sequence. At this stage most mixtures were found to be within 0.5% from critical.

An estimate of the instrumental mass bias is required for critical mixture double spiking[19]. We obtained this estimate from the unspiked DSM-3 analyses in the analysis sequence by dividing the measured $^{25/24}$Mg by the reference $^{25/24}$Mg of 0.12663[35]. Although this can also be done on $^{26/24}$Mg, we find that $^{25/24}$Mg is a more reproducible indicator of mass bias because it is less affected by incomplete

wash-out due to the smaller contrast between the unspiked and spiked ratios. These instrumental mass bias factors were linearly or quadratically interpolated based on the evolution of DSM-3 – double-spike mixtures to obtain a close mass bias approximation for the sample – double-spike mixtures. Once the mass bias estimate was obtained, the analyses were run through a double-spike inversion routine, followed by a normalisation of sample isotope compositions to DSM-3 isotope compositions (obtained from double-spike – DSM-3 mixtures) to correct for residual non-exponential mass fractionation in the instrument.

Our observations are that the mass bias rarely varies by >0.5‰/amu during a 20 h sequence and that this variation tends to be characterized by a smooth evolution. Therefore, we conservatively estimate that the interpolated mass bias is accurate to ≤0.25‰/amu. Combined with our criterion of double-spike proportions being ≤0.5% from critical, we calculate that our Mg isotope compositions should be accurate to better than 0.005‰ on $^{25}Mg/^{24}Mg$[19]. Note that this accuracy estimate is distinct from the reported uncertainty, which is determined from the scatter of replicates.

We have also analysed USGS geological reference material BHVO-2 with a deviation from a critical spike proportion of -1% (overspiked) and +1% (underspiked). The means of these samples are -0.092±0.007‰ and -0.090±0.007‰, respectively. They are hence not significantly different at this level of precision, giving further confidence that our ±0.5% mixing bound is sufficiently tight for accurate results.

Previously published data measured on key reference samples scatter beyond their *2se* uncertainties[18]. Assuming sample homogeneity, this scatter highlights the distinction between accuracy and precision, which cannot be assessed separately in the traditional standard-sample bracketing procedure used by those studies. Whilst some of the data may thus appear precise, they can still be inaccurate. In contrast, we have assessed that our new critical double spiking technique should be accurate within our quoted precision. Hence, application of our technique should reduce the scatter in potential future studies from that observed in Extended Data Figure 5 to within the error bounds of the isotope ratios found in this study, assuming sample homogeneity. Nonetheless, much of the literature data has $\delta^{25/24}Mg$ consistent with our critically double spiked measurements at a ±0.25‰ level (Extended Data Figure 5).

N-body collisional accretion simulations

Our N-body collisional accretion simulations have previously been published[23] and the reader is referred to the original publication for model details. These simulations were ideally suited for our investigations because they included growth of planetary bodies from ~10^{-4} to ~10^{-1} $M_\oplus$ with imperfect accretion. We used two different modes of the high resolution simulations[23], which include i) a calm disk, and ii) the Grand Tack[30]. Whilst we did not modify the simulations in any manner, we extracted additional information (notably impact parameters) to compute accretional vapour loss by two different mechanisms.

435 *1. Impact vaporisation*

436 This information was obtained following published vapour fraction equations (assuming molten
437 basalt)[4]. The equations enabled determining vapour mass (M_{vap}) as a fraction of the impactor mass
438 (M_{imp}) in each collision. The vapour mass fraction in each collision (f_{vap}) was calculated from the
439 impact velocity and angle (v_{imp} and θ), which we have obtained from the N-body simulations
440 (correcting for the expanded radii that were used in these simulations to increase the collision rate):
441 $f_{vap} = M_{vap}\left(v_{imp}\sin\theta\right)/M_{imp}$. The vapour fraction in each collision was subsequently integrated
442 over all collisions a body experienced, taking into account that each planetesimal has its own
443 collisional history, to obtain the fraction of material that experienced impact induced volatilisation
444 relative to the total mass of a body: $F = (1/M)\int_0^M f_{vap}\left(v_{imp}\sin\theta\right)dm$. This equation is modified from
445 the original[4] by replacing the $v_{esc}(m)$ term, which was a proxy for impact velocity, by the impact
446 velocities (v_{imp}) obtained in our N-body simulations. This replacement resulted in higher volatilisation
447 fractions in our study compared to Dauphas et al.[4], particularly for the Grand Tack simulation in which
448 higher impact velocities occur due to dynamical excitation by Jupiter's migration. We obtained Figure
449 2 by binning the results for F in groups of masses (relative to Earth's mass $M_\oplus$) in each of the two
450 simulation modes.
451
452 *2. Vapour mass loss by direct outflow above exposed magma ponds*

453 *Summary:* The overall picture is as follows. We use the impact information from the N-body
454 collisional accretion simulations and let each impact generate a hemispheric pool of melt. Vapour
455 forms above the melt pool, with a pressure determined by the melt pool temperature. The melt vapour
456 escapes at a rate determined by its temperature and the gravity of the body. The melt pool is assumed
457 to be convecting vigorously, keeping it isothermal, and it cools from the surface due to evaporation
458 and radiative heat transfer. As the melt cools, the vapour pressure drops and the vapour mass loss rate
459 decreases until it effectively stops.

460 This overall behaviour is described by an energy equation as follows:

461 $$mC_p\dot{T} = \dot{m}\left(\frac{GM}{R_s} + L_v\right) + A\sigma T_{eff}^4 \qquad (1)$$

462 where the left-hand side denotes the energy source (secular cooling of the melt pool) and the right-
463 hand side denotes the energy sinks (evaporative cooling, gravitational potential energy and radiative
464 heat transfer). Here m is the mass of the melt pool, C_p is its specific heat capacity, $\dot{T}$ is the cooling
465 rate of the melt pool, $\dot{m}$ is the vapour mass loss rate, M is the mass of the body, R_s is its radius, G is
466 the gravitational coefficient, L_v is the latent heat of vaporization, σ is Stefan's constant, T_{eff} is the
467 effective radiating temperature of the melt pool and A is its surface area. We take C_p =1200 $Jkg^{-1}K^{-1}$,
468 L_v=5 MJ kg^{-1} and the magma density and body bulk density to both be 3000 kgm^{-3}.

Below we describe the different energy sources and sinks, and our calculation methods, in more detail. We have deliberately tried to keep our approach relatively simple, but even so there are a large number of parameters, some of which are highly uncertain. That being the case, a more complicated model seems premature; our main aim is to demonstrate that vapour loss from melt ponds is a plausible mechanism for generating vapour mass loss, and thereby isotopic fractionation.

Mass loss rate: Atmospheres which have a gas thermal velocity comparable to the escape velocity of the body are vulnerable to loss by direct outflow[36]. For Earth-mass bodies the thermal velocity required is implausibly high (except perhaps for close-in "roaster" planets that may occur in exoplanetary systems[37]) but for small bodies this requirement is less restrictive. The resulting outflow can be described by the equations of mass and momentum conservation:

$$\frac{1}{\rho}\frac{d\rho}{dr}+\frac{1}{v}\frac{dv}{dr}+\frac{2}{r}=0 \qquad (2)$$

$$\frac{1}{\rho}\frac{dP}{dr}+v\frac{dv}{dr}=-\frac{GM}{r^2} \qquad (3)$$

where r is the radial coordinate, $P(T)$, $\rho(T)$ and v are the pressure, density and radial velocity of the gas and we are assuming spherical geometry. For an ideal gas we have $R'T = P/\rho = v_s^2$ where R' is the gas constant divided by the molar mass, T is the gas temperature and v_s is the sound speed. To close the system, we also need an energy equation. The simplest, which we will adopt here, is to assume an isothermal atmosphere with the temperature set by the melt pool surface temperature T. A more realistic description would be to assume a vapour-saturated atmosphere; Lehmer et al.[38] have shown that this latter system is actually well-approximated by the isothermal description.

Under these assumptions, the gas will accelerate outwards until it reaches the "sonic point" at which $v=v_s$. At this critical radius r_c the sonic velocity is half the local escape velocity, with

$$r_c = \frac{GM}{2R'T} = R_s\left(\frac{v_{esc}}{2v_s}\right)^2$$

and v_{esc} is the escape velocity at the body surface ($r=R_s$). The atmospheric mass loss rate is then given by $4\pi r_c^2 \rho(r_c) v_s$. Given the surface density, equations (2) and (3) may then be integrated outwards to calculate $\rho(r_c)$ and thus the mass loss rate. For small bodies, r_c may be equal to or less than R_s, in which case the mass loss rate is $4\pi R_s^2 \rho(R_s) v_s$. In our case the gas density at the surface $\rho(r_s)$ is set by the vapour pressure of the melt pool. Because only the melt pool is losing vapour, we replace $4\pi R_s^2$ with A, the melt pool area, in our mass loss calculations. We assume a molar mass of 0.04 kg/mol, appropriate for MgO or SiO.

Driving mass loss requires energy because of two effects (equation 1): conversion of liquid to vapour takes latent heat, and removal of mass from the surface to large distances involves potential energy changes. We consider both these effects in more detail below.

Secular cooling and radiative heat transfer: Secular cooling of the melt pool provides the energy to drive mass loss. The melt pool is assumed isothermal (temperature T) due to vigorous convection. This temperature sets the gas vapour pressure at the surface. Here we take the vapour pressure to be given by the following empirical expression obtained from our thermodynamic liquid-vapour model (see below):

$$\ln P = -4.0041\ (\ln T)^3 + 88.788\ (\ln T)^2 - 639.3 \ln T + 1480.23$$

where P is in bars.

An important aspect of our model is that the effective radiating temperature of the melt pool T_{eff} is lower than the temperature T which sets the gas vapour pressure and defines the internal temperature of the melt. This effect is observed at terrestrial lava lakes, where the surface temperature is typically many hundreds of K cooler[39] than the measured subsurface magma temperature and that inferred from the gas equilibrium chemistry[40]. A similar effect is found at Io, where the majority of a lava lake's surface is at much lower temperature than the expected magma temperature[41].

The reason for this effect is that there is a thin conductive skin on top of the convecting magma, which is at a lower temperature than the material beneath. To approximately describe this phenomenon, we set the heat flux conducted across this layer equal to the heat flux radiated from the top surface:

$$F = \frac{k(T - T_{eff})}{\delta} = \sigma T_{eff}^4$$

where k is the thermal conductivity and δ is the skin thickness. This allows us to solve for T_{eff} given T and δ. To calculate δ we assume the convecting melt pool can be described by isoviscous convection[42]

$$\delta \approx 2\left(\frac{\kappa\eta}{\rho g \alpha [T - T_{eff}]}\right)^{1/3}$$

At high temperatures, the dominant energy sink in equation (1) is evaporative cooling, because radiative heat loss increases as T^4, while mass loss (which depends on the vapour pressure) increases exponentially with T. Thus, the overall mass loss calculations are not particularly sensitive to the details of the radiative cooling calculations.

Here we take α=3x10^{-5} K^{-1}, η=10^3 Pa s. The thermal conductivity k is taken to be 3 Wm^{-1} K^{-1} which then specifies κ. For T=1400 K and a 1000 km radius body we find T_{eff}=853 K, which is roughly consistent with terrestrial lava lake measurements[39].

Melt pool volume and temperature: To calculate the melt pool volume and temperature we assume that the volume of material shocked to the maximum temperature (the isobaric core) is hemispherical and has a radius linearly proportional to the impactor radius: $R_{ic} = f\ R_i$, with f=3 following literature[4,43]. Assuming that some fraction of the kinetic energy of the impactor is consumed within this volume, the temperature change associated with impact is then given by

$$\Delta T = \frac{1}{C_p}\left[\left(\frac{R_i}{R_{ic}}\right)^3 \beta {v_{imp}}^2 - L_m\right] \quad (4)$$

where L_m is the latent heat of fusion, v_{imp} is the impact velocity (given by the N-body simulations) and β is a factor to account for energy delivered beyond the isobaric core. Here we take β=0.5 to provide a conservative estimate of the initial melt temperature. Inspection of this equation shows that a minimum velocity of about 4.6 km/s is required to initiate significant mass loss.

We assume that the pre-impact target material is at the solidus, here taken to be 1400 K. The justification for doing so is that heating by ^{26}Al will melt bodies that formed early enough (to be conservative, we ignore at this stage that such melting induced by ^{26}Al heating could have led to vapour mass loss). Melt advection will rapidly cool the target to 1400 K, but subsequent cooling (by conduction or solid-state convection) will be much slower. We also impose a maximum melt temperature of 3500 K. This is approximately the temperature at which total silicate vaporization is achieved and the physics of mass loss will change. Imposing this cut-off will underestimate the total amount of mass loss.

Although the radius of the isobaric core is somewhat uncertain, varying f does not have a very large effect on our results, because of the trade-offs involved. A smaller isobaric core reduces the surface area and cooling timescale, but it increases the melt temperature (and thus the vapour pressure and the initial mass loss rate). By contrast, the difference between regular and Grand Tack accretion is dramatic. This is because the Grand Tack results in more dynamical excitation, and thus more energetic collisions.

Extended Data Figure 6 plots the median impact velocity normalized to the escape velocity as a function of body radius. The biggest difference between a calm disk (without gas drag) and Grand Tack accretion is that the normalized impact velocities for large bodies are much bigger in the latter. Since no vapour loss happens below a particular cut-off velocity (equation 4), it is clear that Grand Tack simulations will generate much more vapour loss. Increasing β to 1 causes only modest increases in the predicted mass loss for conventional accretion, because impact velocities are still general below the cut-off value.

Implementation: Each body undergoes mass growth by collision; each collision may also lead to some mass loss via vapour outflow. For each impact, we calculate the initial melt pool mass and temperature as outlined in the section *Melt pool volume and temperature*. The instantaneous mass loss rate is calculated using as described in the section *Mass loss rate*. Given the mass loss rate, the change in melt pool temperature is calculated according to equation (1). The temperature is updated accordingly and the cycle then repeats. The total mass lost is tracked.

A disadvantage of our approach is that the pre-history of impactors striking a target body is not recorded. Since these impactors have likely undergone mass loss of their own, our approach may therefore underestimate the total fractional mass loss of the final body. To mitigate this problem, for the Grand Tack results we perform a two-step calculation. In the first step we calculate the total mass

loss for each body neglecting inheritance effects. We use these results to determine the median mass loss over all bodies within a particular final mass range. The median prior fractional mass loss ϕ determined in this manner for the GT bodies is given by the following empirical formula:

$$\phi = 0.4\times10^{-5} R_s^{1.65} e^{-0.65\times10^{-5} R_s^{1.65}}$$

where R_s is in km. We then re-run the calculations, this time assuming that each impactor has experienced prior mass loss based on this median value. The results of both calculations are shown in Extended Data Figure 7.

For the conventional accretion simulations without gas present in the disk ("calm disk") vapour loss is sufficiently small that we neglected this inheritance effect. Extended Data Figure 7 plots the median fractional mass loss for all bodies in the Grand Tack accretion simulations. The simulations for a calm disk result in very limited mass loss, and only for the largest (see Figure 2b in main text). By contrast, mass loss in the Grand Tack scenario is much more extensive.

Vapour-liquid Mg isotope fractionation models

We first consider a kinetic isotope fractionation scenario. For this, we modelled the elemental loss of Mg required to obtain ~0.02‰ heavier Mg isotope compositions by a Rayleigh distillation process with an experimentally determined kinetic isotope fractionation factor[44] (referred to as $\alpha^{25/24}Mg^{kin}_{g/liq}$) of 0.9860. We obtained a relative mass loss of Mg by vaporization (f^{vap}_{Mg}) of 0.14% from $f^{vap}_{Mg} = 1 - e^{\delta^{25/24}Mg/\left(\alpha^{25/24}Mg^{kin}_{g/liq}-1\right)}$. This is a very small mass loss, but we can expect much larger concomitant K mass losses, owing to its higher volatility. Although it is hard to quantify such K loss, we can estimate it from an equilibrium liquid-vapour model (see below), given that kinetic evaporative fluxes (J) from a molten surface are proportional to their saturation vapour pressures as well as the elemental mass[44]. In the simplest scenario, i.e. assuming a single vaporisation event, we find 0.14% of Mg is vaporised at ~2700 K, at which temperature ~28% of K occurs as vapour (all as atomic K). Using a published[45] $\alpha^{40/39}K^{kin}_{g/liq}$ of 0.9892 we obtain that $^{41}K/^{39}K$ fractionates by ~7‰. This compares to <2.7±1‰ observed fractionation in Solar System material[25], underscoring the implausibility of kinetic fractionation.

We also examine an equilibrium liquid-vapour fractionation model. Vapour production results in isotopically light vapour and heavy liquid compositions, thus evolving a vapour depleted bulk planetesimal to isotopically heavier compositions. The composition of silicate vapour in equilibrium with a molten planetesimal was calculated with a thermodynamic model involving equilibrium reactions between silicate liquid and vapour species for nine elements: O, Na, Mg, Al, Si, K, Ca, Ti and Fe. The model is modified from the MAGMA code by Fegley and co-workers[46,47]. We followed the approach of these authors to non-ideal mixing in the silicate liquid (i.e. assuming ideal mixing of complex oxide and silicate pseudo-components), used their tabulated thermodynamic data, and, like

them, we assumed ideal mixing in the gas. Our approach differs from theirs in that we let go of their constraint that oxygen-to-metal ratios in the gas must be identical to the original liquid. Instead, we used the ideal gas law to convert partial pressures of gas species to number of moles in order to enforce conservation of mass by simultaneously solving mass balance equations for the number of moles of each element. Hence, we have 66 equilibrium equations and nine mass balance equations to solve for activities of 75 species. The disadvantage of our approach is that the ideal gas law adds one freely adjustable parameter in the form of the volume the gas can expand into. We have chosen to fix this volume such that vapour fractions between ~0.001 and ~0.15 were obtained between 2500 K and 3500 K. Such fractions are of similar order of magnitude to the average vapour fraction produced in single collisions in the N-body simulations (note that an order of magnitude variation in the chosen volume leads to ~5 fold variation in the vapour fractions but these changes do not affect our conclusions because their effect is counterbalanced by the number of "collisions" that are run to obtain the observed Mg isotope composition; see below). To convert from activities of the liquid species to moles, which we need for the mass balance equations, we need one more variable, i.e. the total moles of all liquid species, bringing the number of unknowns to 76. However, there is the activity normalisation constraint: the activities (i.e. mole fractions) of liquid species must sum to 1. Hence, we have 76 constraints to solve for 76 variables. The code is easily expandable with extra elements and equilibrium reactions and is freely available from the authors upon request.

In our equilibrium liquid-vapour fractionation model, we used published reduced partition functions (β) to approximate equilibrium Mg, Si and Fe isotope fractionation factors between silicate liquid and atomic silicate vapour. Experimental calibrations of equilibrium isotope fractionation factors between vapour and liquid do not exist to date. As β are currently unavailable for silicate liquid, we approximated them with those for forsterite crystals for Mg[48] and Si[49] and fayalite crystals for Fe[50]. We used further literature sources for β for other vapour species $MgO_{(g)}$[48], $FeO_{(g)}$[51] and $SiO_{(g)}$[49,52]. Relative abundances of species in mixed vapours, e.g. Mg(g) and MgO(g), were obtained from the thermodynamic model described above. A two-component mass balance relationship combining isotope compositions of the vapour (subscript *g*) and the remaining 'liquid' (subscript *liq*) were used to determine the offset relative to the original bulk composition (set to 0 for reference here) prior to loss of a vapour fraction (f_g): $\delta^{25/24}Mg_{liq} = -f_g \delta^{25/24}Mg_g \Big/ \left(1 - f_g\right)$.

We used this equilibrium vapour-liquid fractionation model to simulate vapour loss as various temperature events (i.e. planetary collisions). We initiated the model with a chondritic elemental composition (see main text) and isotope compositions of 0, as mentioned above. We removed 95% of the chondritic Fe assuming it segregated into a core which is not affected by vaporisation. We let a single "collision" affect 20% of the body and assumed that the body undergoes full chemical homogenisation between two events. After the first "collision", the calculated isotopic and elemental compositions of the residual liquid were then used as initial values for the next "collision", and so forth. The temperature used to calculate equilibrium vapour-liquid compositions and isotopic

fractionation in any "collision" event was obtained by random selection of a temperature uniformly distributed between 2500 K and 3500 K.

Additional references

32 Galy, A. *et al.* Magnesium isotope heterogeneity of the isotopic standard SRM980 and new reference materials for magnesium-isotope-ratio measurements. *J. Anal. At. Spectrom.* **18**, 1352-1356, doi:10.1039/b309273a (2003).

33 Coplen, T. B. Guidelines and recommended terms for expression of stable-isotope-ratio and gas-ratio measurement results. *Rapid Commun Mass Sp* **25**, 2538-2560, doi:10.1002/rcm.5129 (2011).

34 Regelous, M., Elliott, T. & Coath, C. D. Nickel isotope heterogeneity in the early Solar System. *Earth Planet. Sci. Lett.* **272**, 330-338, doi:10.1016/j.epsl.2008.05.001 (2008).

35 Catanzaro, E. J., Murphy, T. J., Garner, E. L. & Shields, W. R. Absolute isotopic abundance ratios and atomic weight of magnesium. *Journal of Research of the National Bureau of Standards Section - A Physics and Chemistry* **70A**, 453-458 (1966).

36 Pierrehumbert, R. T. *Principles of planetary climate*. (Cambridge University Press, 2010).

37 Perez-Becker, D. & Chiang, E. Catastrophic evaporation of rocky planets. *Mon Not R Astron Soc* **433**, 2294-2309, doi:10.1093/mnras/stt895 (2013).

38 Lehmer, O. R., Catling, D. C. & Zahnle, K. J. The longevity of water ice on Ganymedes and Europas around migrated giant planets. *The Astrophysical Journal* **839**, 32-40, doi:10.3847/1538-4357/aa67ea (2017).

39 Patrick, M. R., Orr, T., Swanson, D. A. & Lev, E. Shallow and deep controls on lava lake surface motion at Kīlauea Volcano. *J. Volcanology Geothermal Res.* **328**, 247-261, doi:10.1016/j.jvolgeores.2016.11.010 (2016).

40 Moussallam, Y. *et al.* Hydrogen emissions from Erebus volcano, Antarctica. *B. Volcanol.* **74**, 2109-2120, doi:10.1007/s00445-012-0649-2 (2012).

41 Davies, A. G. *Volcanism on Io: A comparison with Earth*. (Cambridge University Press, 2007).

42 Solomatov, V. S. Scaling of temperature- and stress-dependent viscosity convection. *Physics of Fluids* **7**, 266-274, doi:10.1063/1.868624 (1995).

43 Melosh, H. J. *Impact cratering: A geologic process*. (Oxford University Press, 1989).

44 Richter, F. M., Janney, P. E., Mendybaev, R. A., Davis, A. M. & Wadhwa, M. Elemental and isotopic fractionation of Type B CAI-like liquids by evaporation. *Geochim. Cosmochim. Acta* **71**, 5544-5564, doi:10.1016/j.gca.2007.09.005 (2007).

45 Richter, F. M., Mendybaev, R. A., Christensen, J. N., Ebel, D. & Gaffney, A. Laboratory experiments bearing on the origin and evolution of olivine-rich chondrules. *Meteorit. Planet. Sci* **46**, 1152-1178, doi:10.1111/j.1945-5100.2011.01220.x (2011).

46 Fegley, B. & Cameron, A. G. W. A vaporization model for iron/silicate fractionation in the Mercury protoplanet. *Earth Planet. Sci. Lett.* **82**, 207-222, doi:10.1016/0012-821x(87)90196-8 (1987).

47 Schaefer, L. & Fegley, B. A thermodynamic model of high temperature lava vaporization on Io. *Icarus* **169**, 216-241, doi:10.1016/j.icarus.2003.08.023 (2004).

48 Schauble, E. A. First-principles estimates of equilibrium magnesium isotope fractionation in silicate, oxide, carbonate and hexaaquamagnesium(2+) crystals. *Geochim. Cosmochim. Acta* **75**, 844-869, doi:10.1016/j.gca.2010.09.044 (2011).

49 Huang, F., Wu, Z. Q., Huang, S. C. & Wu, F. First-principles calculations of equilibrium silicon isotope fractionation among mantle minerals. *Geochim. Cosmochim. Acta* **140**, 509-520, doi:DOI 10.1016/j.gca.2014.05.035 (2014).

50 Polyakov, V. B. & Mineev, S. D. The use of Mössbauer spectroscopy in stable isotope geochemistry. *Geochim. Cosmochim. Acta* **64**, 849-865, doi:10.1016/S0016-7037(99)00329-4 (2000).

51 Pahlevan, K. *Chemical and isotopic consequences of lunar formation via giant impact* PhD thesis, Califoria Institute of Technology, (2010).
52 Javoy, M., Balan, E., Méheut, M., Blanchard, M. & Lazzeri, M. First-principles investigation of equilibrium isotopic fractionation of O- and Si-isotopes between refractory solids and gases in the solar nebula. *Earth Planet. Sci. Lett.* **319**, 118-127, doi:10.1016/j.epsl.2011.12.029 (2012).
53 Clayton, R. N. & Mayeda, T. K. Oxygen isotope studies of carbonaceous chondrites. *Geochim. Cosmochim. Acta* **63**, 2089-2104, doi:10.1016/S0016-7037(99)00090-3 (1999).
54 Van Schmus, W. R. & Wood, J. A. A chemical-petrologic classification for the chondritic meteorites. *Geochim. Cosmochim. Acta* **31**, 747-765, doi:10.1016/S0016-7037(67)80030-9 (1967).
55 Sossi, P. A., Nebel, O. & Foden, J. Iron isotope systematics in planetary reservoirs. *Earth Planet. Sci. Lett.* **452**, 295-308, doi:10.1016/j.epsl.2016.07.032 (2016).
56 O'Neill, H. S. C. & Palme, H. Collisional erosion and the non-chondritic composition of the terrestrial planets. *Phil. Trans. Roy. Soc. A* **366**, 4205-4238, doi:10.1098/rsta.2008.0111 (2008).
57 Badro, J. *et al.* Effect of light elements on the sound velocities in solid iron: Implications for the composition of Earth's core. *Earth Planet. Sci. Lett.* **254**, 233-238, doi:10.1016/j.epsl.2006.11.025 (2007).
58 Hin, R. C., Fitoussi, C., Schmidt, M. W. & Bourdon, B. Experimental determination of the Si isotope fractionation factor between liquid metal and liquid silicate. *Earth Planet. Sci. Lett.* **387**, 55-66, doi:10.1016/j.epsl.2013.11.016 (2014).
59 Armytage, R. M. G., Georg, R. B., Savage, P. S., Williams, H. M. & Halliday, A. N. Silicon isotopes in meteorites and planetary core formation. *Geochim. Cosmochim. Acta* **75**, 3662-3676, doi:10.1016/j.gca.2011.03.044 (2011).
60 Schiller, M., Handler, M. R. & Baker, J. A. High-precision Mg isotopic systematics of bulk chondrites. *Earth Planet. Sci. Lett.* **297**, 165-173, doi:10.1016/j.epsl.2010.06.017 (2010).
61 Schiller, M., Baker, J. A. & Bizzarro, M. ^{26}Al-^{26}Mg dating of asteroidal magmatism in the young Solar System. *Geochim. Cosmochim. Acta* **74**, 4844-4864, doi:10.1016/j.gca.2010.05.011 (2010).
62 Larsen, K. K. *et al.* Evidence for Magnesium Isotope Heterogeneity in the Solar Protoplanetary Disk. *Astrophys J Lett* **735**, doi:10.1088/2041-8205/735/2/L37 (2011).

Data availability

Source data for Table 1 and all Figures not generated by modelling data have been provided with the paper. Data generated by modelling code can be made available from the corresponding author upon reasonable request. Magnesium isotope compositions generated in this study are available in the EarthChem repository.

Extended Data Table and Figure captions

Extended Data Table 1. Sample sources and weights of digested sample from which aliquots were taken for Mg isotope analysis in this study. NHM is Natural History Museum, London, UK. NASA is National Aeronautics and Space Administration. [1]Aliquot from a homogenised powder of several grams.

Extended Data Figure 1. Magnesium isotope compositions of carbonaceous chondrites plotted against their average literature oxygen isotope compositions[53]. These mass-dependent oxygen isotope measurements reflect parent body hydrothermal alteration[20], so the correlation ($R^2 = 0.78$) between Mg and O isotopes (as well as with petrographic group[54]; indicated in brackets under sample names) implies that the Mg isotope compositions of some carbonaceous chondrites have been altered by hydrothermal processes. The most altered samples, to the upper right of this diagram, are excluded from our chondrite Mg isotope means.

Extended Data Figure 2. Magnesium isotope compositions of peridotites plotted against whole rock MgO (panel a) and Al_2O_3 (panel b) contents. The absence of correlations of Mg isotope compositions with MgO or Al_2O_3 indicates absence of discernible Mg isotope fractionation during partial melting.

Extended Data Figure 3. Comparison between modelled compositions of a vapour depleted liquid and observed planetary compositions. As Figure 3 in main text, but additionally including observed isotope compositions for Mars, and eucrite and angrite parents bodies as well as including elemental and isotopic Fe observations (panels b and d; Fe isotope data from [55] and references therein, all other references as in Figure 3). Comparison of observed Fe contents and isotope ratios are complicated by core formation because most Fe enters the core. In our model we assume that the iron in the core has not been affected by vaporisation, inferred to occur later. For instance, the effect of ~48% Fe loss (panel c) on the current bulk silicate Earth Fe content is dependent on the fraction of Fe that entered the core prior to collisional vaporisation and the oxygen fugacity evolution of the growing Earth. For reference, the datum labelled Fe** in panel d is therefore the Fe/Ca of the bulk Earth (calculated from [56]) instead of the Fe/Ca of the bulk silicate Earth. Similarly, Si can also enter the

768 core, although its quantity is likely <3 wt%[57]. Right pointing arrows in b) and d) indicate the effect of
769 3 wt% Si in the core (3000 K assumed for metal-silicate Si isotope fractionation factor[58]).
770
771 Extended Data Figure 4. Comparison between modelled compositions of a vapour depleted liquid
772 and observed planetary compositions. Similar to Extended Data Figure 3, but for model runs with a CI
773 chondrite initial composition. Observed Mg and Fe isotope compositions (panel b) are presented
774 relative chondrite mean, while Si isotope observations are relative to a mean of carbonaceous and
775 ordinary chondrites[59], because those chondrites have undistinguishable Si isotope compositions, yet
776 are distinctly different from enstatite chondrites (see [4] and references therein).
777
778 Extended Data Figure 5. Magnesium isotope compositions of reference samples analysed in
779 multiple studies. The shaded areas show the mean and 2se of the isotope compositions observed in this
780 study. Note that the plotted composition of Murchison for Bourdon et al.[10] is a mean of the two
781 replicates presented in their Table 1. The value for BHVO of Chakrabarti and Jacobsen[16] is BHVO-1,
782 all others are BHVO-2.
783
784 Extended Data Figure 6. Variation in velocity of individual impacts (normalized by target body
785 escape velocity) as a function of target body radius. Central line denotes median value, shaded box
786 encompasses region spanning 25th-75th percentiles, upper lines denote 90th percentile. Bulk density
787 assumed to be 3000 kg m^{-3}.
788
789 Extended Data Figure 7. Fractional mass loss in Grand Tack simulation as a function of final body
790 radius for direct vapour outflow model to illustrate results both with (white boxes, as Figure 2b) and
791 without (shaded boxes) the inclusion of inheritance effects (see Methods). Boxes denote the median
792 value, bars denote the 25th and 75th quartiles.
793

794

795 Table 1. Magnesium isotope compositions of chondrites, terrestrial (ultra-)mafics, and achondrites.

Sample	Type	δ^{25}Mg (‰)	2se	n[1]
Orgueil	CI1	-0.105	0.010	8
Ivuna	CI1	-0.095	0.008	12
Al Rais	CR2	-0.094	0.008	12
Renazzo	CR2	-0.135	0.008	12
Kainsaz	CO3	-0.158	0.010	8
Murchison	CM2	-0.145	0.010	8
Parnallee	LL3	-0.152	0.009	11
Dhurmsala	LL6	-0.148	0.010	8
Ceniceros	H3	-0.157	0.009	11
Zag	H3	-0.132	0.007	19,2
Khairpur	EL6	-0.137	0.006	23,2
Hvittis	EL6	-0.135	0.008	12
Yilmia	EL6	-0.130	0.007	16
St Mark's	EH5	-0.129	0.006	23,2
Abee	EH4	-0.142	0.008	12
Indarch	EH4	-0.128	0.008	12
Mean Chondrites[2]		*-0.140*	*0.006*	
JP-1	Dunite	-0.117	0.004	43,5
BZ116	Sp Hz	-0.133	0.009	11
Vi 313-102	Gt Lz	-0.130	0.010	8
BZ143	Sp Lz	-0.120	0.009	11
BZ-29	Sp Lz	-0.115	0.010	8
Vi 314-56	Sp Lz	-0.115	0.010	8
BZ251	Plg Lz	-0.129	0.010	8
2370-1	MORB	-0.111	0.010	8
DS12-29	MORB	-0.110	0.010	8
9/30a(1)	MORB	-0.124	0.010	8
BIR-1	OIB	-0.099	0.010	8
BHVO-2	OIB	-0.095	0.004	60,3
Mean Earth[3]		*-0.121*	*0.005*	
ALHA 77005	Lz Sherg	-0.112	0.009	11
DaG 476	Bas Sherg	-0.123	0.009	11
EETA 79001	Bas Sherg	-0.113	0.009	11
RBT 04262	Ol Sherg	-0.117	0.010	8
Zagami	Bas Sherg	-0.113	0.010	8
LAR 06319	Ol Sherg	-0.102	0.009	11
Mean Mars		*-0.113*	*0.006*	
Johnstown	Diogenite	-0.102	0.010	8
Shalka	Diogenite	-0.104	0.010	8
Tatahouine	Diogenite	-0.127	0.010	8
Mean Diogenites		*-0.111*	*0.016*	
d'Orbigny	Angrite	-0.079	0.010	8

[1] Total number of analyses. If a comma is present, the number behind the comma refers to the number of digestions. Each digestion was passed through chemistry once.

[2] The two CI1 chondrites (Ivuna, Orgueil) and one CR2 (Al Rais) were excluded from the mean.

[3] The two Ocean Island Basalts (BHVO-2 and BIR-1) were excluded from the mean.

Sp Hz = Spinel Harzburgite, Gt Lz = Garnet Lherzolite, Plg = Plagioclase, MORB = Mid-Ocean Ridge Basalt, OIB = Ocean Island basalt, Bas Sherg = Basaltic Shergottite, Ol = Olivine-phyric.

796

797

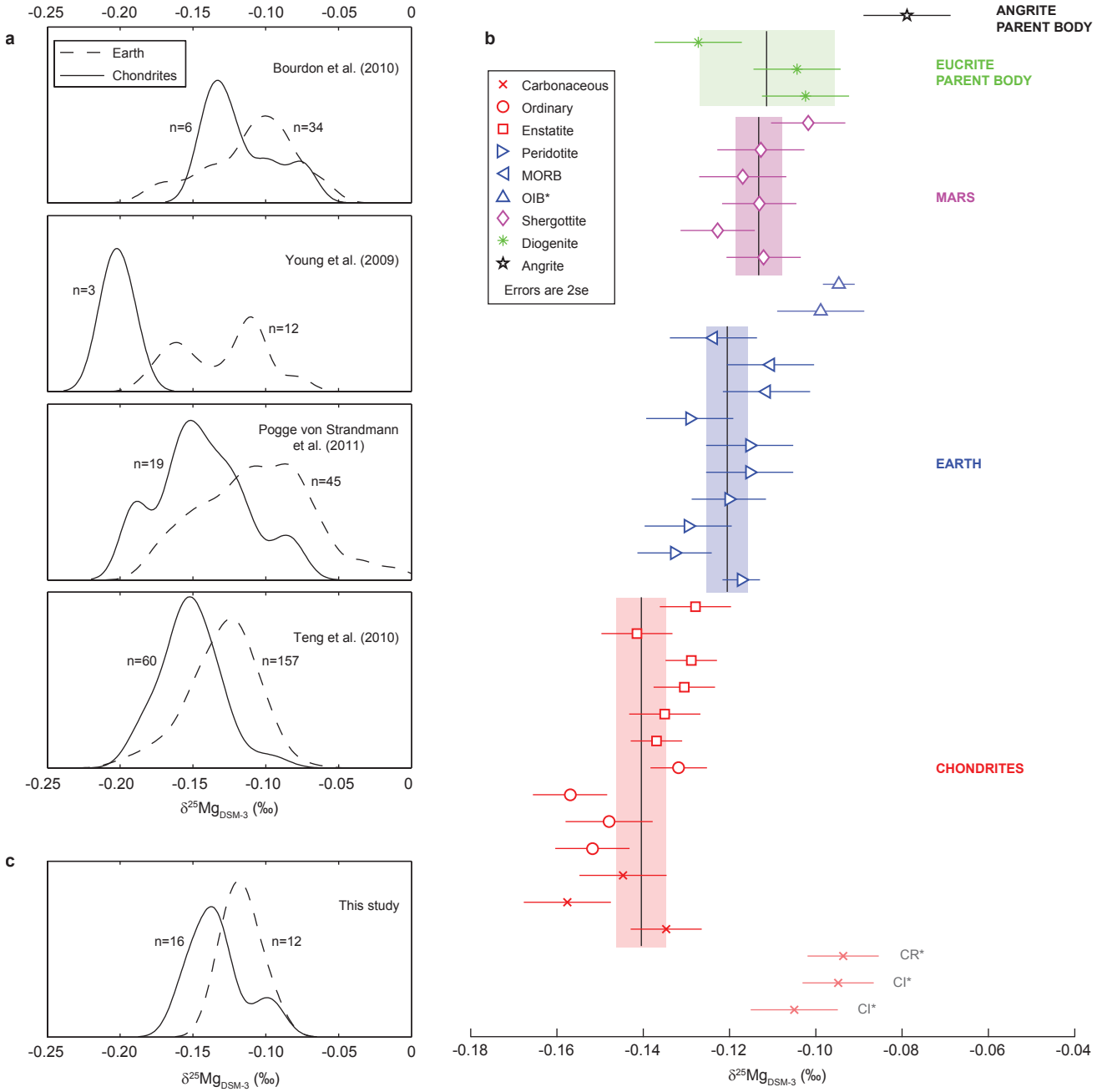
a
Earth
Chondrites
Bourdon et al. (2010)
n=6
n=34
Young et al. (2009)
n=3
n=12
Pogge von Strandmann et al. (2011)
n=19
n=45
Teng et al. (2010)
n=60
n=157
-0.25 -0.20 -0.15 -0.10 -0.05 0
δ25MgDSM-3 (‰)
b
Carbonaceous
Ordinary
Enstatite
Peridotite
MORB
OIB*
Shergottite
Diogenite
Angrite
Errors are 2se
ANGRITE PARENT BODY
EUCRITE PARENT BODY
MARS
EARTH
CHONDRITES
CR*
CI*
CI*
-0.18 -0.16 -0.14 -0.12 -0.10 -0.08 -0.06 -0.04
δ25MgDSM-3 (‰)
c
This study
n=16
n=12
-0.25 -0.20 -0.15 -0.10 -0.05 0
δ25MgDSM-3 (‰)

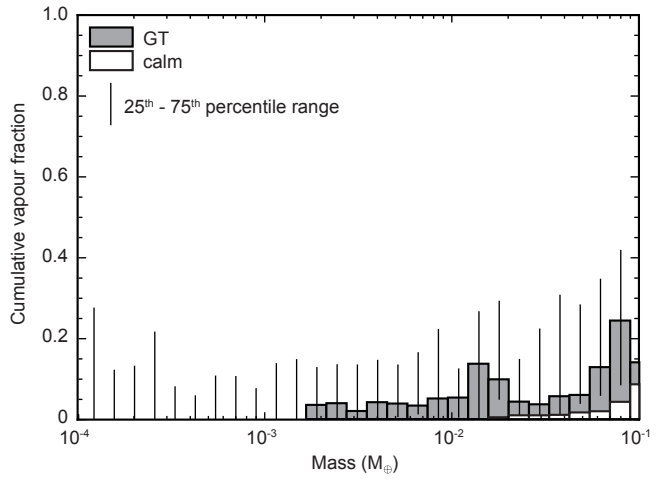
GT
calm
25th - 75th percentile range
Cumulative vapour fraction
Mass (M⊕)

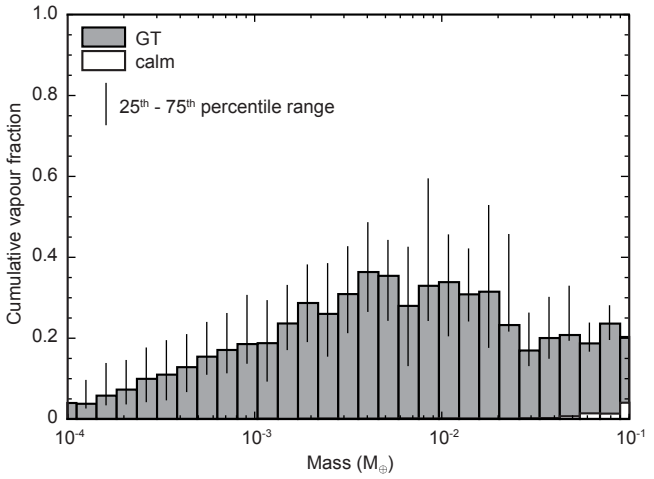
GT
calm
25th - 75th percentile range
Cumulative vapour fraction
Mass (M⊕)

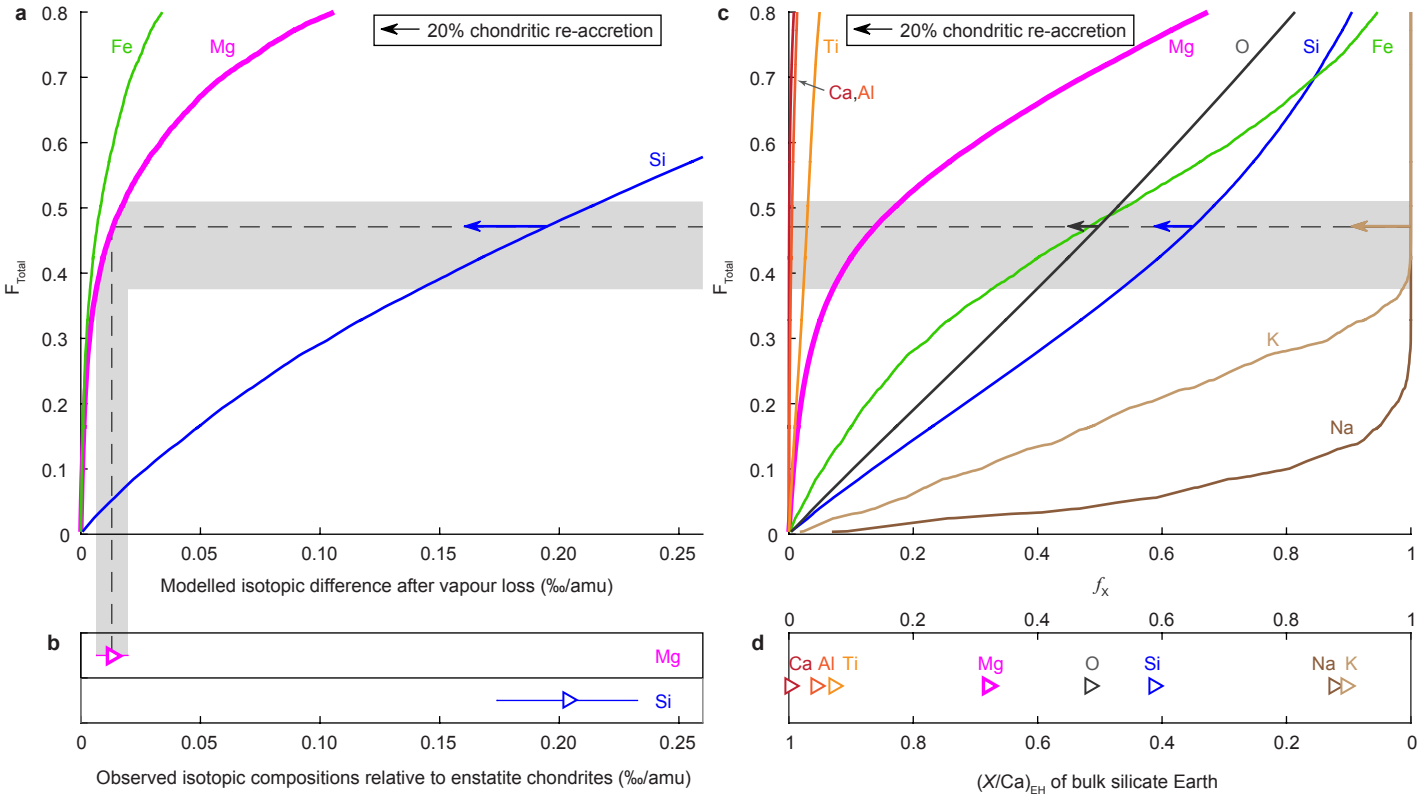
a
b
c
d
20% chondritic re-accretion
Fe
Mg
Si
Ti
Ca,Al
O
K
Na
F_Total
Modelled isotopic difference after vapour loss (‰/amu)
Observed isotopic compositions relative to enstatite chondrites (‰/amu)
f_x
(X/Ca)_EH of bulk silicate Earth

Meteorites	Source	Sample weight digested (mg)	Identification number
Orgueil	NMH	98.14	BM 36104
Ivuna	NHM	11.6	BM 1991, M5
Al Rais	NHM	4.6	BM 1971, 289
Renazzo	NHM	4.4	BM 41105
Kainsaz	NMH	69.34	BM 1988,M24
Murchison	NMH	86.92	BM 1970,6
Parnallee	NMH	6.37	BM 34792
Dhurmsala	NHM	12.69	BM 96262
Ceniceros	NMH	46.93	BM 1989,M31
Zag	Meteorite dealer	7.18[1]	-
Khairpur	NMH	69.39	BM 51366
Hvittis	NHM	45.8	BM 86754
Yilmia	NHM	29.8	BM 1972, 132
St Mark's	NMH	60.37	BM 1990, 339
Abee	NHM	66.7	BM 1997, M7
Indarch	NHM	97.0	BM 1921, 23
ALHA 77005	NASA	71.99	ALHA77 005, 234
DaG 476	Meteorite dealer	91.78	-
EETA 79001	NASA	121.19	EETA79 001, 665
RBT 04262	NASA	89.09	RBT 04 262, 61
Zagami	Meteorite dealer	61.00	-
LAR 06319	NASA	95.58	LAR 06 319, 59
Johnstown	NHM	133.31	BM 1959,828
Shalka	NHM	155.58	BM 33761
Tatahouine	NHM	112.89	BM1931,490
d'Orbigny	Meteorite dealer	15.28[1]	-
Terrestrial			Location
BZ116	ref 51	7.89[1]	Bozu section, Horoman peridotite, Japan
Vi 313-102	ref 52	23.97[1]	Vitim volcanic field, Russia
BZ143	ref 51	4.23[1]	Bozu section, Horoman peridotite, Japan
BZ-29	ref 53	12.97[1]	Zabargad Island, Egypt
Vi 314-56	ref 52	10.39[1]	Vitim volcanic field, Russia
BZ251	ref 51	11.93[1]	Bozu section, Horoman peridotite, Japan
2370-1	ref 54	3.39	9-10°N East Pacific Rise
DS12-29	ref 55	3.92	26°S Mid-Atlantic Ridge
9/30a(1)	ref 56	2.07	57°E South-West Indian Ridge

[1]Aliquot from a homogenised powder of several grams

NHM = Natural History Museum

NASA = National Aeronautics and Space Administration

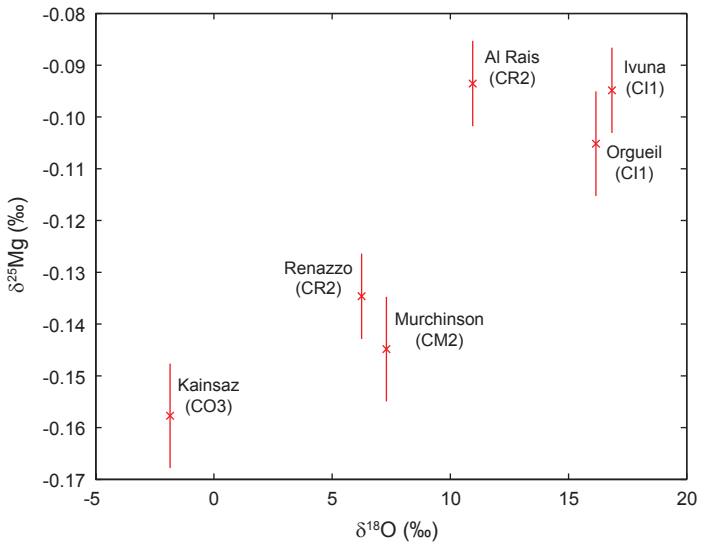
-0.08
-0.09
-0.10
-0.11
-0.12
-0.13
-0.14
-0.15
-0.16
-0.17
-5
0
5
10
15
20
δ25Mg (‰)
δ18O (‰)
Al Rais
(CR2)
Ivuna
(CI1)
Orgueil
(CI1)
Renazzo
(CR2)
Murchinson
(CM2)
Kainsaz
(CO3)

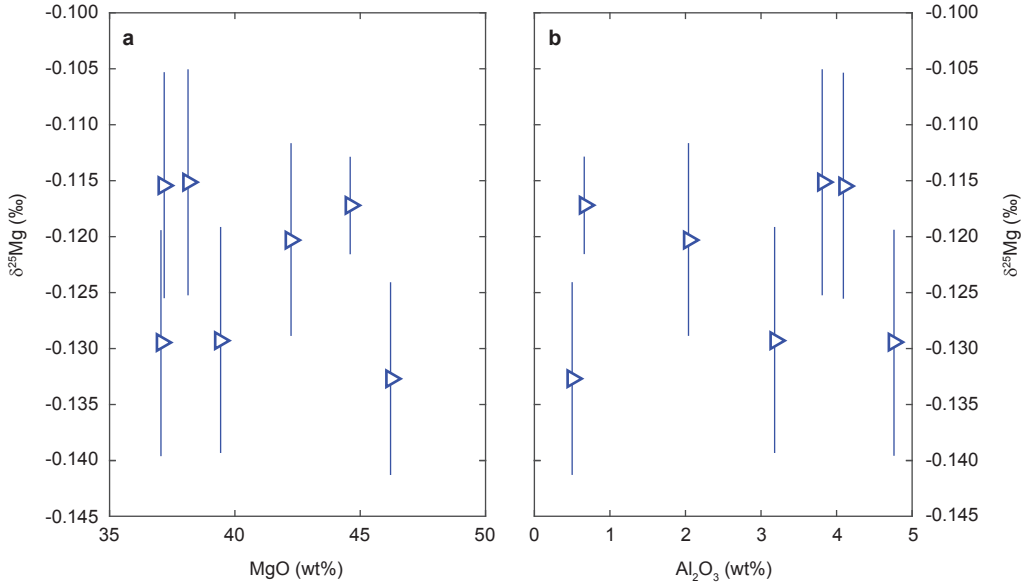
a
b
-0.100
-0.105
-0.110
-0.115
-0.120
-0.125
-0.130
-0.135
-0.140
-0.145
δ25Mg (‰)
35
40
45
50
MgO (wt%)
0
1
2
3
4
5
Al2O3 (wt%)

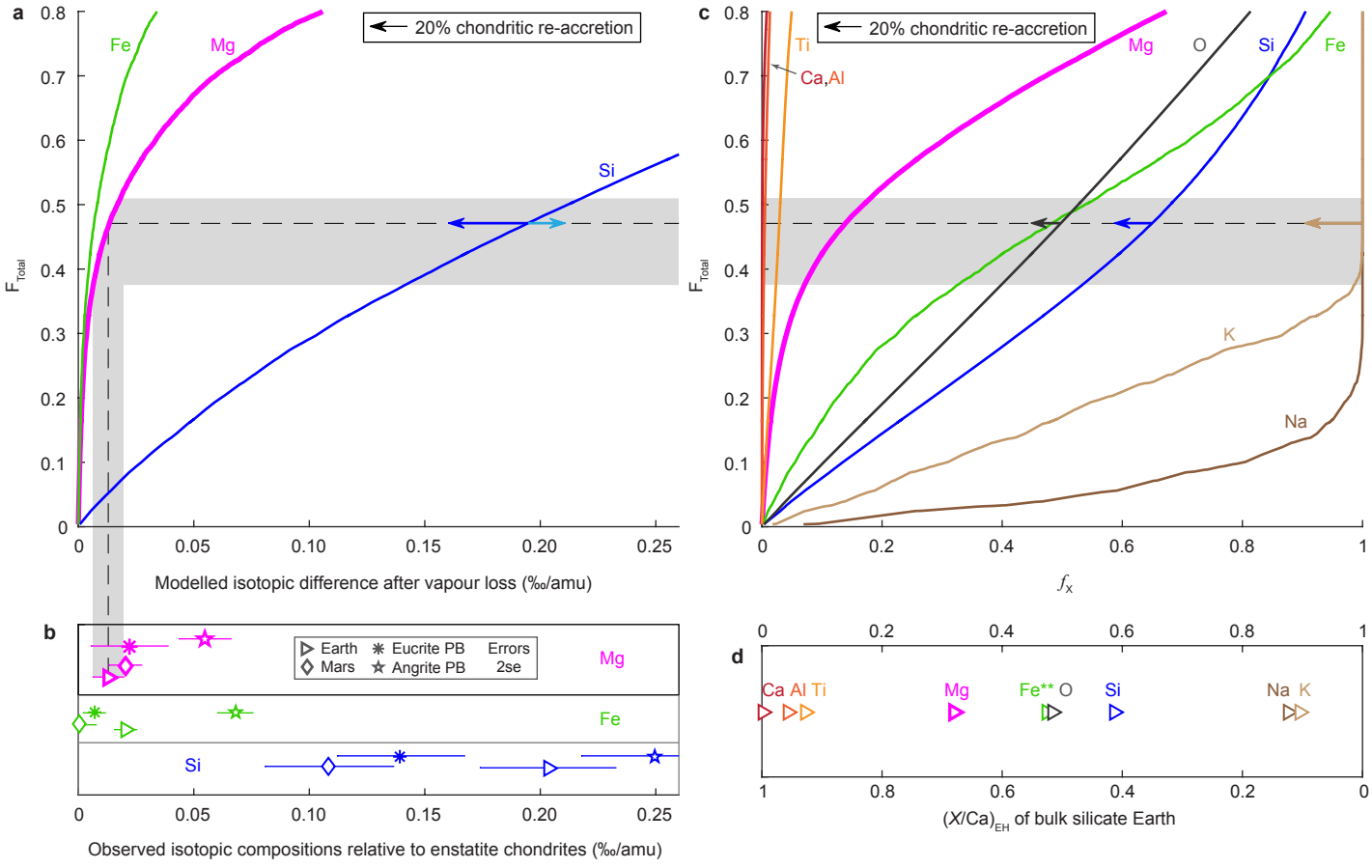
a
20% chondritic re-accretion
Fe
Mg
Si
F_Total
Modelled isotopic difference after vapour loss (‰/amu)
b
Earth
Mars
Eucrite PB
Angrite PB
Errors
2se
Mg
Fe
Si
Observed isotopic compositions relative to enstatite chondrites (‰/amu)
c
20% chondritic re-accretion
Ti
Ca,Al
Mg
O
Si
Fe
K
Na
F_Total
f_x
d
Ca Al Ti
Mg
Fe** O
Si
Na K
(X/Ca)_EH of bulk silicate Earth

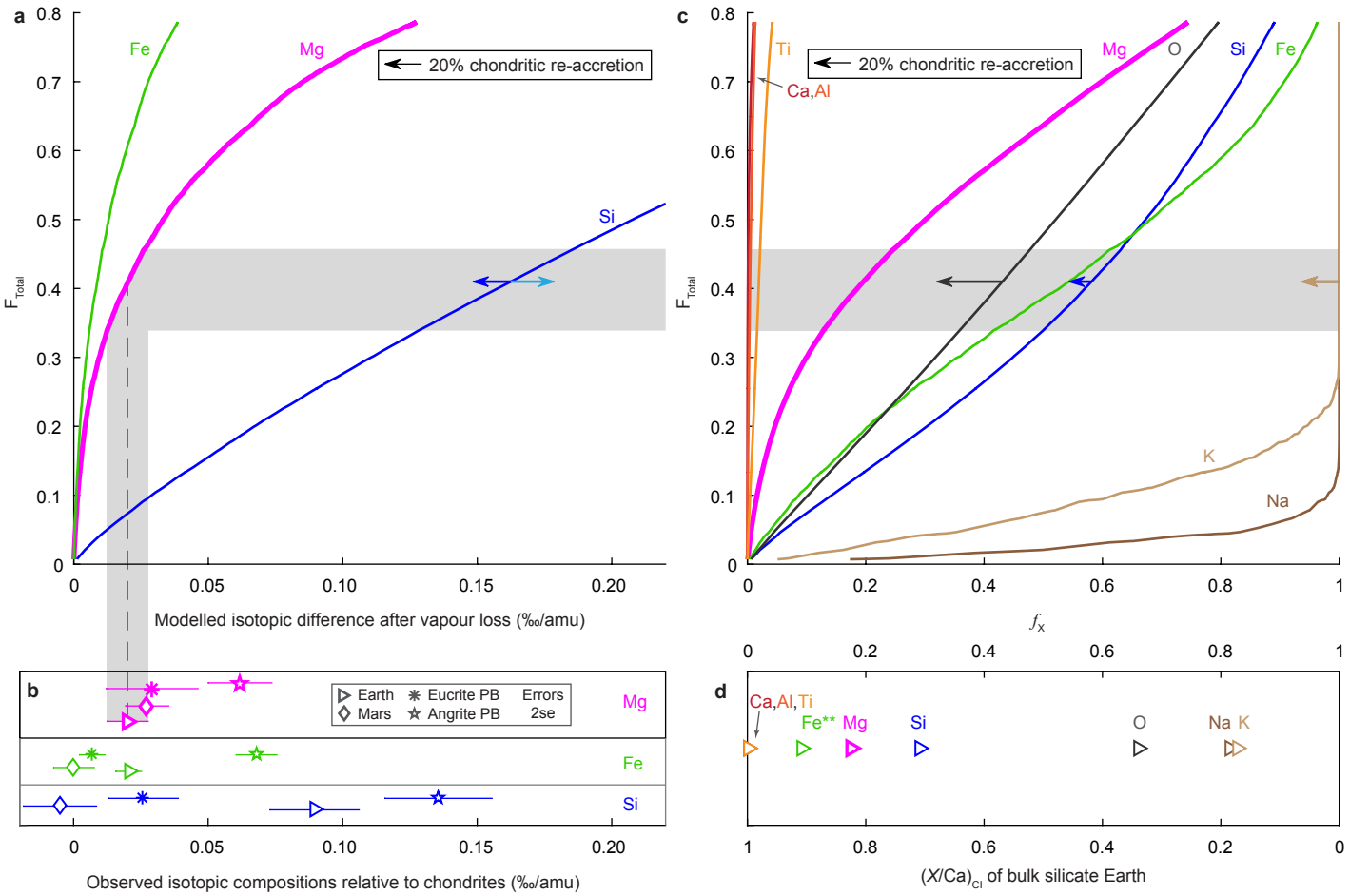
a
c
b
d
Fe
Mg
Si
Ti
Ca,Al
O
K
Na
20% chondritic re-accretion
F_Total
Modelled isotopic difference after vapour loss (‰/amu)
f_x
Earth
Mars
Eucrite PB
Angrite PB
Errors
2se
Observed isotopic compositions relative to chondrites (‰/amu)
Fe**
(X/Ca)_CI of bulk silicate Earth

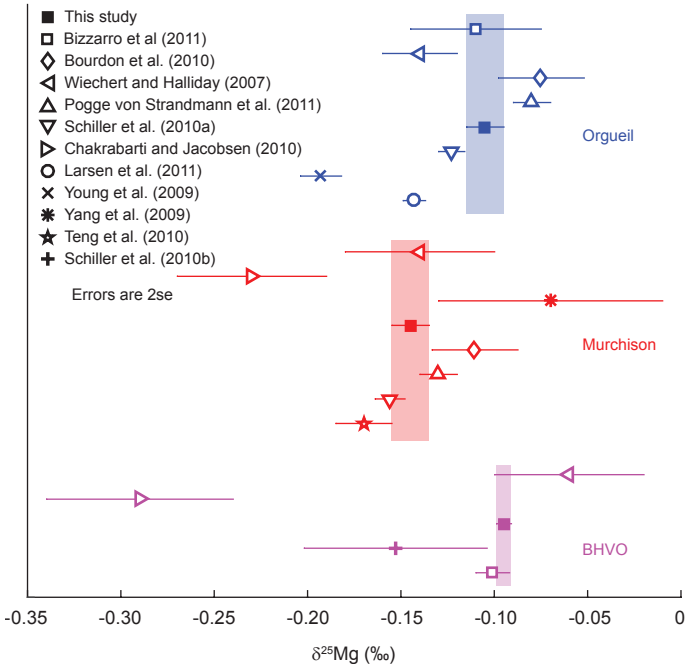
This study
Bizzarro et al (2011)
Bourdon et al. (2010)
Wiechert and Halliday (2007)
Pogge von Strandmann et al. (2011)
Schiller et al. (2010a)
Chakrabarti and Jacobsen (2010)
Larsen et al. (2011)
Young et al. (2009)
Yang et al. (2009)
Teng et al. (2010)
Schiller et al. (2010b)
Errors are 2se
Orgueil
Murchison
BHVO
-0.35
-0.30
-0.25
-0.20
-0.15
-0.10
-0.05
0
δ25Mg (‰)

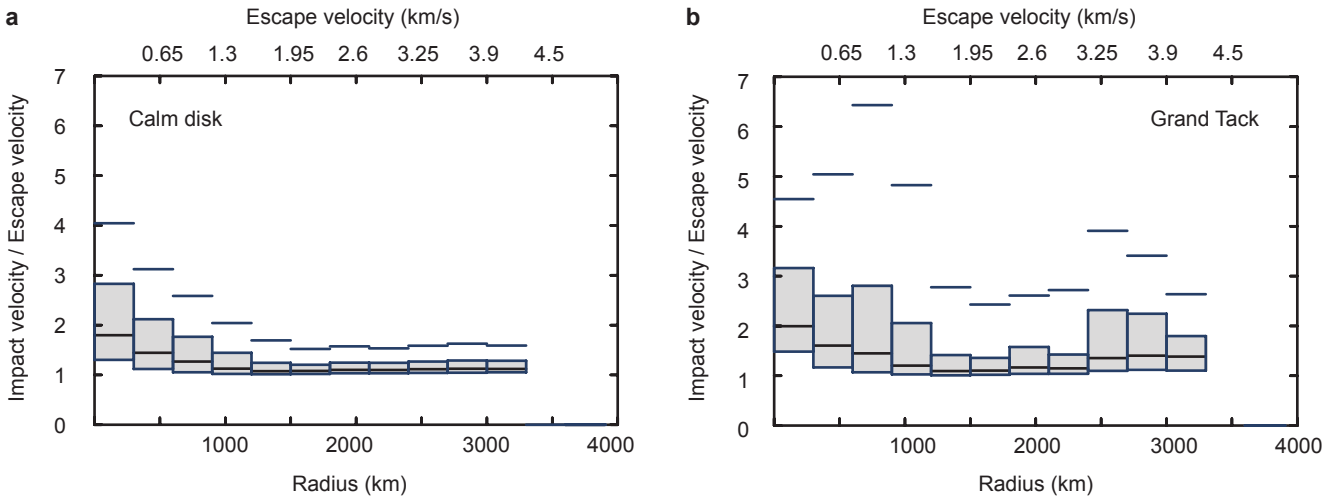
a
Escape velocity (km/s)
0.65 1.3 1.95 2.6 3.25 3.9 4.5
Calm disk
Impact velocity / Escape velocity
0 1 2 3 4 5 6 7
1000 2000 3000 4000
Radius (km)
b
Escape velocity (km/s)
0.65 1.3 1.95 2.6 3.25 3.9 4.5
Grand Tack
Impact velocity / Escape velocity
0 1 2 3 4 5 6 7
1000 2000 3000 4000
Radius (km)

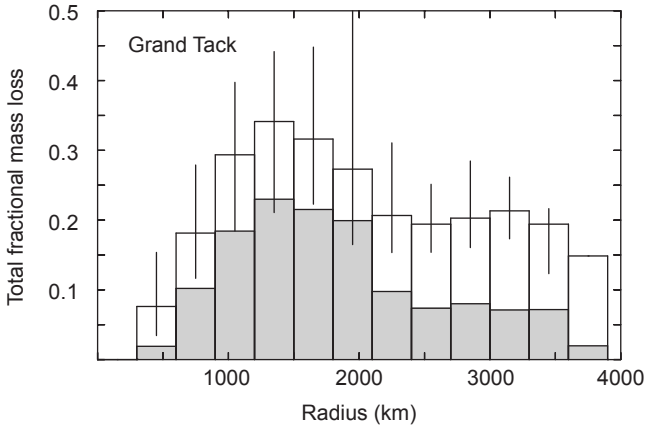
Grand Tack
Total fractional mass loss
0.5
0.4
0.3
0.2
0.1
1000
2000
3000
4000
Radius (km)